Supplemental Information for:

Secondary organic aerosol formation from in situ OH, O_3, and NO_3 oxidation of ambient forest air in an oxidation flow reactor

Brett B. Palm[1,2], Pedro Campuzano-Jost[1,2], Amber M. Ortega[1,3,+], Douglas A. Day[1,2], Juliane L. Fry[4], Steven S. Brown[2,5], Kyle J. Zarzana[1,2,*], William Dube[1,5], Nicholas L. Wagner[1,5], Danielle C. Draper[4,#], Lisa Kaser[6], Werner Jud[7,^], Thomas Karl[8], Armin Hansel[7], Cándido Gutiérrez-Montes[9], and Jose L. Jimenez[1,2]

[1]Cooperative Institute for Research in Environmental Sciences, University of Colorado, USA;
[2]Department of Chemistry and Biochemistry, University of Colorado, USA;
[3]Department of Atmospheric and Oceanic Science, University of Colorado, USA;
[4]Department of Chemistry, Reed College, USA;
[5]NOAA Earth System Research Laboratory, Chemical Sciences Division, Boulder, CO, USA
[6]National Center for Atmospheric Research, USA;
[7]Institute of Ion Physics and Applied Physics, University of Innsbruck, Austria;
[8]Institute of Atmospheric and Cryospheric Sciences, University of Innsbruck, Austria;
[9]Departamento de Ingeniería, Mecánica y Minera, Universidad de Jaen, Jaen, Spain
[+]Now at Air Pollution Control Division, Colorado Department of Public Health and Environment, Denver, CO, USA
**Now at NOAA Earth System Research Laboratory, Chemical Sciences Division, Boulder, CO, USA*
[#]Now at Department of Chemistry, University of California, Irvine, USA
^Now at Research Unit Environmental Simulation (EUS), Institute of Biochemical Plant Pathology (BIOP), Helmholtz Zentrum München GmbH, Germany

S1 NO_3 oxidant modeling

To estimate NO_3 exposure in the OFR when injecting N_2O_5, the KinSim chemical-kinetic integrator (version 3.10) was used. Table S1 contains the reactions and rate constant parameters implemented in the model. The model was run with a residence time calculated from the total measured flow in the OFR (between 150 and 240 s). The model was run using this research site's ambient pressure of 770 mbar, and was initialized with measurements of ambient temperature, RH, O_3 concentrations, monoterpene (MT) concentrations, a constant 0.15 ppb NO, and injected NO_2, NO_3, and N_2O_5 concentrations for each data point. The N_2O_5 wall loss rate constant k_{wall}, shown in Fig. S4a, was empirically determined to have a base value of 0.014 s^{-1} (lifetime of 71 s) using the measured N_2O_5 difference between the injection flow and OFR output concentrations while injecting N_2O_5 into dry zero air in the reactor. Using measurements when injecting into ambient air, an empirical increase in this wall loss rate was required when RH was greater than 80% in order to reproduce the concentrations of N_2O_5 injected and remaining in the OFR output (see Fig. 2a). Figure S4b shows the modeled vs. measured N_2O_5 remaining, illustrating the need for the increasing wall loss rate at high RH. The base wall loss rate of 0.014 s^{-1} is several times faster than

the wall loss rate of 0.0025 s^{-1} estimated in Palm et al. (2016) for condensable organic gases (LVOCs) produced by oxidation in the OFR. This empirical result may be a consequence of the N_2O_5 flow being injected through a Teflon ring that was mounted close to the OFR wall, increasing the effective surface-area-to-volume ratio experienced by the injected N_2O_5. Injection near the wall may also have been the cause for the relatively large increase in wall loss rate at high RH. The N_2O_5 wall loss rate also implicitly includes any losses on the sampling line walls after the OFR, which also had higher surface-area-to-volume ratios that would likely lead to larger apparent loss rates. The NO_3 wall loss rate was assumed to be equal to the N_2O_5 wall loss rate (and has little effect on the key model outputs). The rate constant for reactive uptake of N_2O_5 onto particulate water surfaces, k_{aer}, is shown as a function of RH in Fig. S5. It was calculated using the measured ambient aerosol condensational sink using the same method described for condensation of LVOCs onto aerosols in Palm et al (2016), except using an organic-mass-fraction-corrected uptake efficiency $\gamma(N_2O_5)$ from Gaston et al. (2014). This heterogeneous uptake was typically several orders of magnitude slower than the wall loss rate, and was therefore a minor loss pathway for N_2O_5.

Time constraints prevented the full characterization of the flow characteristics of the experimental setup during the field measurements. Instead, PTR-TOF-MS measurements of the decay of ambient MT in the OFR were used to parameterize the mixing process. With relatively robust constraints provided by measurements of N_2O_5, NO_2, and NO_3, the model results make it clear that a well-mixed OFR would contain more than enough NO_3 to react virtually all ambient biogenic gases, if gases were immediately well-mixed. However, the PTR-TOF-MS measurements verified that substantial amounts of MT often remained in the OFR output. Incomplete mixing of the injected N_2O_5 was the most likely explanation for this observation. A parameterization for the time constant needed for mixing of the injected N_2O_5 flow with ambient air at the entrance of the OFR was added to the model to provide an effective empirical mixing time scale of 100 s. This parameterization for mixing has the same effect as the high wall loss rates of N_2O_5, which is to decrease the concentrations of oxidant experienced by MT inside the reactor. The true time scale of mixing and wall loss rate may be somewhat different, but the model results presented herein suggest the values used in this work capture the net behavior satisfactorily. The time series of measured and modeled MT decay are shown in Fig. S6–7, which are in addition to the example given in Fig. 4.

References

Atkinson, R. and Arey, J.: Gas-phase tropospheric chemistry of biogenic volatile organic compounds: a review, Atmos. Environ., 37, 197–219, doi:10.1016/S1352-2310(03)00391-1, 2003.

Atkinson, R., Baulch, D. L., Cox, R. A., Crowley, J. N., Hampson, R. F., Hynes, R. G., Jenkin, M. E., Rossi, M. J. and Troe, J.: Evaluated kinetic and photochemical data for atmospheric chemistry: Volume I - gas phase reactions of O_x, HO_x, NO_x and SO_x species, Atmos. Chem. Phys., 4, 1461–1738, doi:10.5194/acp-4-1461-2004, 2004.

Atkinson, R., Baulch, D. L., Cox, R. A., Crowley, J. N., Hampson, R. F., Hynes, R. G., Jenkin, M. E., Rossi, M. J., Troe, J. and IUPAC Subcommittee: Evaluated kinetic and photochemical data for atmospheric chemistry: Volume II - gas phase reactions of organic species, Atmos. Chem. Phys., 6, 3625–4055, doi:10.5194/acp-6-3625-2006, 2006.

Gaston, C. J., Thornton, J. A. and Ng, N. L.: Reactive uptake of N_2O_5 to internally mixed inorganic and organic particles: the role of organic carbon oxidation state and inferred organic phase separations, Atmos. Chem. Phys., 14, 5693–5707, doi:10.5194/acp-14-5693-2014, 2014.

Lambe, A. T., Ahern, A. T., Williams, L. R., Slowik, J. G., Wong, J. P. S., Abbatt, J. P. D., Brune, W. H., Ng, N. L., Wright, J. P., Croasdale, D. R., Worsnop, D. R., Davidovits, P. and Onasch, T. B.: Characterization of aerosol photooxidation flow reactors: heterogeneous oxidation, secondary organic aerosol formation and cloud condensation nuclei activity measurements, Atmos. Meas. Tech., 4, 445–461, doi:10.5194/amt-4-445-2011, 2011.

Palm, B. B., Campuzano-Jost, P., Ortega, A. M., Day, D. A., Kaser, L., Jud, W., Karl, T., Hansel, A., Hunter, J. F., Cross, E. S., Kroll, J. H., Peng, Z., Brune, W. H. and Jimenez, J. L.: In situ secondary organic aerosol formation from ambient pine forest air using an oxidation flow reactor, Atmos. Chem. Phys., 16, 2943–2970, doi:10.5194/acp-16-2943-2016, 2016.

Sander, S. P., Abbatt, J. P. D., Barker, J. R., Burkholder, J. B., Friedl, R. R., Golden, D. M., Huie, R. E., Kolb, C. E., Kurylo, M. J., Moortgat, G. K., Orkin, V. L. and Wine, P. H.: Chemical Kinetics and Photochemical Data for Use in Atmospheric Studies Evaluation Number 17, JPL Publ. 10-6, Jet Propulsion Laboratory, California Institute of Technology, Pasadena, CA, USA, 2011.

Tables

Table S1. List of reactions and parameters used in modeling of the oxidant chemistry in the OFR when performing NO_3 oxidation. The rate constants are calculated using the modified Arrhenius equation $k = A \cdot (\frac{T(K)}{300})^{-n} \cdot e^{-\frac{E}{RT(K)}}$ with pressure dependence as described in Sect. 2 of JPL (Sander et al., 2011). Parameter values are from JPL, with exceptions noted.

Reactant 1	Reactant 2	Product 1	Product 2	Product 3	A_∞	E_∞/R	n_∞	A_0	E_0/R	n_0
NO	O_3	NO_2	O_2		3e-12	1500	0	0	0	0
NO_2	O_3	NO_3	O_2		1.2e-13	2450	0	0	0	0
N_2O_5		NO_2	NO_3		9.7e+14[1]	11080	-0.1	0.0013	11000	3.5
N_2O_5		Wall loss			k_{wall}[2]	0	0	0	0	0
NO_3		Wall loss			k_{wall}[2]	0	0	0	0	0
NO_3	α-pinene	RO_2			1.2e-12[1]	-490	0	0	0	0
NO_3	3-carene	RO_2			9.1e-12[1]	0	0	0	0	0
NO_3	β-pinene	RO_2			2.5e-12[1]	0	0	0	0	0
N_2O_5	$H_2O_{(g)}$	HNO_3	HNO_3		1e-22	0	0	0	0	0
N_2O_5	$H_2O_{(aerosol)}$	HNO_3	HNO_3		k_{aer}[2]	0	0	0	0	0
NO	NO_3	NO_2	NO_2		1.8e-11	-110	0	0	0	0
NO_2	NO_3	NO	NO_2	O_2	4.5e-14	1260	0	0	0	0
NO_3	NO_3	NO_2	NO_2	O_2	8.5e-13	2450	0	0	0	0
NO_2	NO_3	N_2O_5			1.9e-12[1]	0	-0.2	3.6e-30	0	4.1
NO_3	RO_2	RO			1.5e-12	0	0	0	0	0
MT mixing source		α-pinene	3-carene	β-pinene	0.01[2]	0	0	0	0	0

[1]Parameter values taken from IUPAC (Atkinson et al., 2004, 2006)

[2]See Sect. S1 for parameter details

Table S2. List of reactions and parameters used in modeling of the oxidant chemistry in the OFR when performing O_3 oxidation. The rate constants are calculated using the modified Arrhenius equation $k = A \cdot (\frac{T(K)}{300})^{-n} \cdot e^{-\frac{E}{T(K)}}$. Parameter values are from IUPAC (Atkinson et al., 2006).

Reactant 1	Reactant 2	Product 1	A	E	n
O_3	α-pinene	Products	8.05×10^{-16}	640	0
O_3	β-pinene	Products	1.35×10^{-15}	1270	0
O_3	3-carene	Products	4.8×10^{-17}	0	0

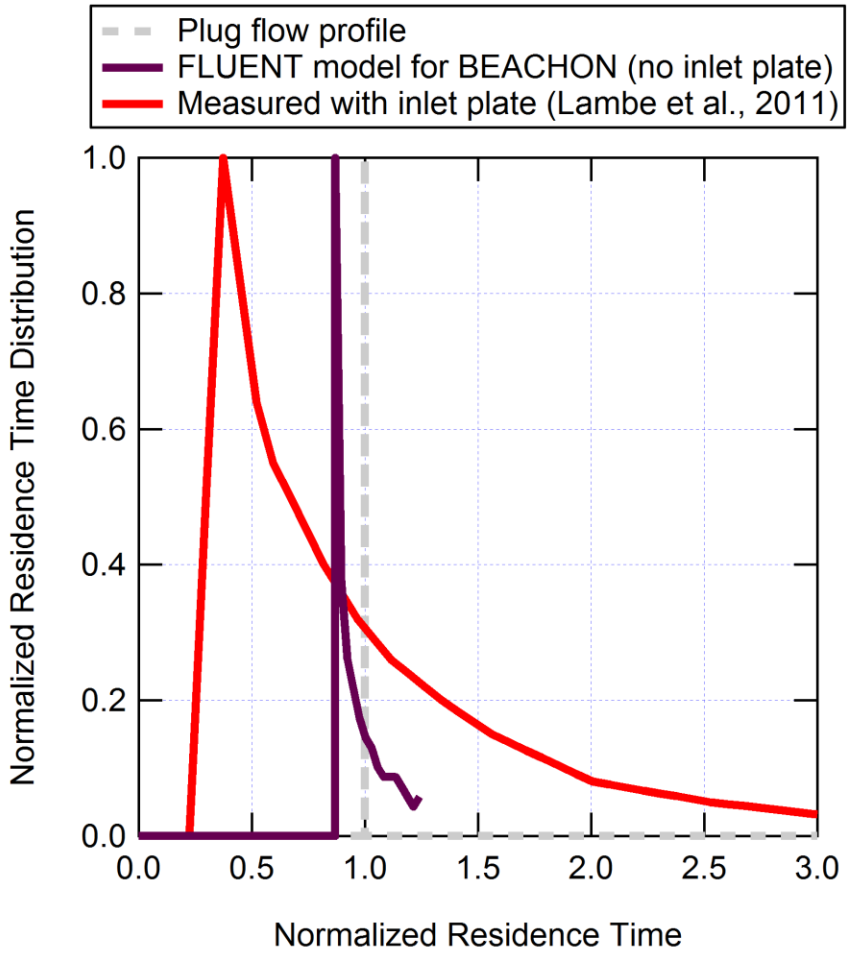

Fig. S1. Normalized residence time distributions in the OFR as a function of normalized residence time (1 = avg. residence time of each distribution). The FLUENT model was used to calculate the residence time for the OFR configuration without the inlet plate used during BEACHON-RoMBAS. This distribution is compared to the bis(2-ethylhexyl) sebacate (BES) particle residence time distribution measured with the inlet plate on in Lambe et al. (2011) and to the ideal plug flow distribution (where all particles have equal residence time calculated as the OFR volume divided by the total flow rate through the OFR). The residence time distribution without the inlet plate is much narrower than with the plate and is close to plug flow, though local winds will create a broader distribution than the model shows.

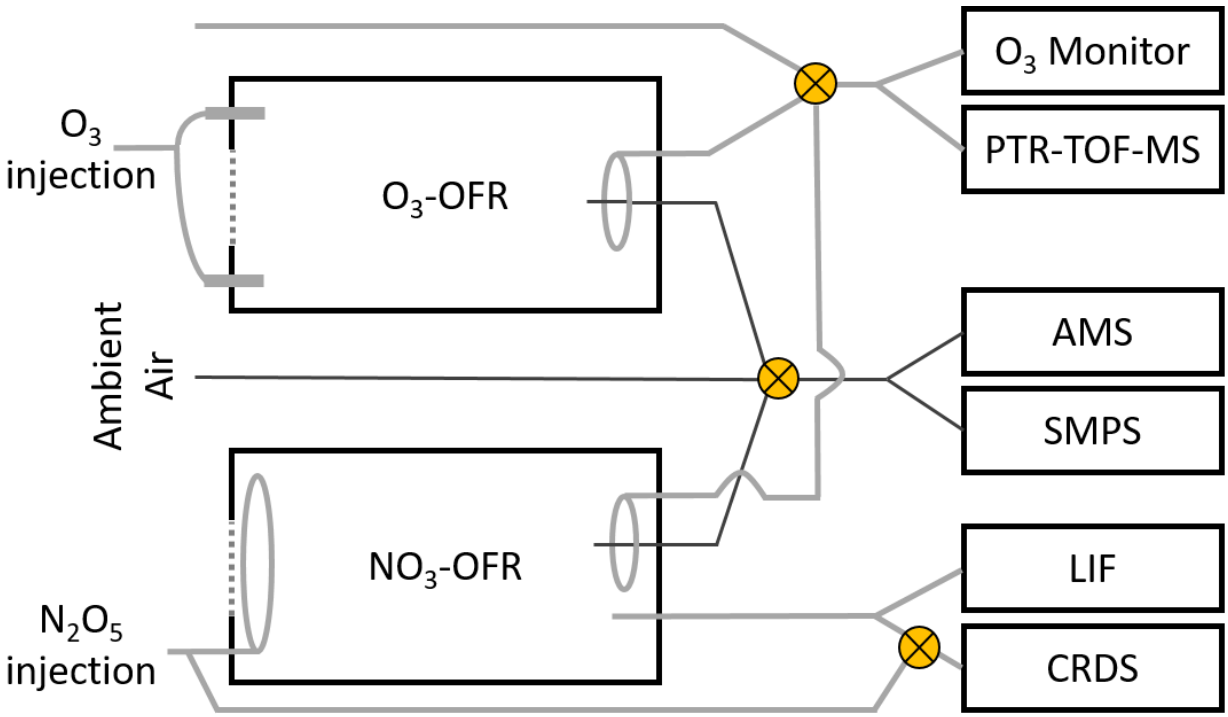

Fig. S2. Schematic of experimental setup of NO_3-OFR and O_3-OFR experiments.

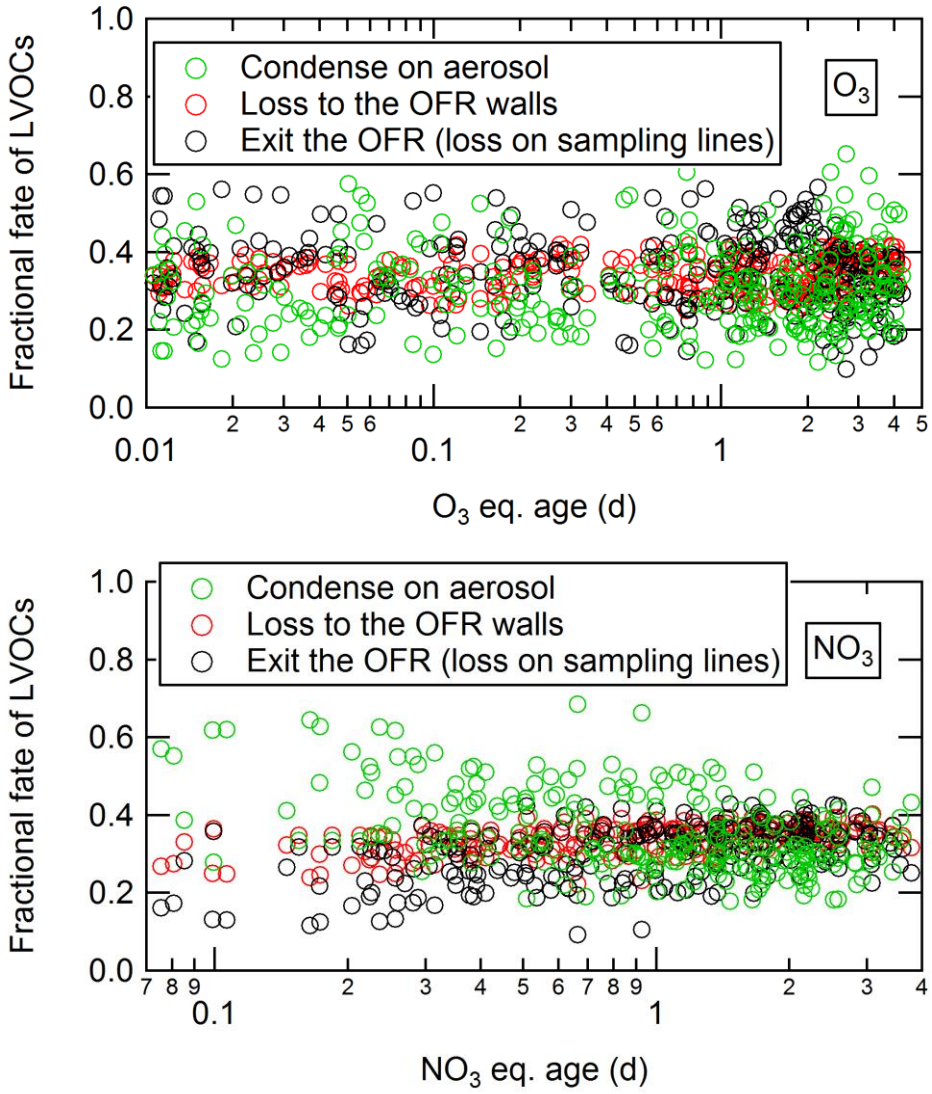

Fig. S3. Fractional fates of condensable low-volatility organic compounds (LVOCs) produced in the OFR, as a function of eq. age for O_3 oxidation (top) and NO_3 oxidation (bottom). For O_3 oxidation, on average 31% of LVOCs condensed onto particles, 34% condensed on OFR walls, and 35% exited the OFR to condense on sampling line walls. For NO_3 oxidation, on average 36% of LVOCs condensed onto particles, 34% condensed on OFR walls, and 30% exited the OFR to condense on sampling line walls.

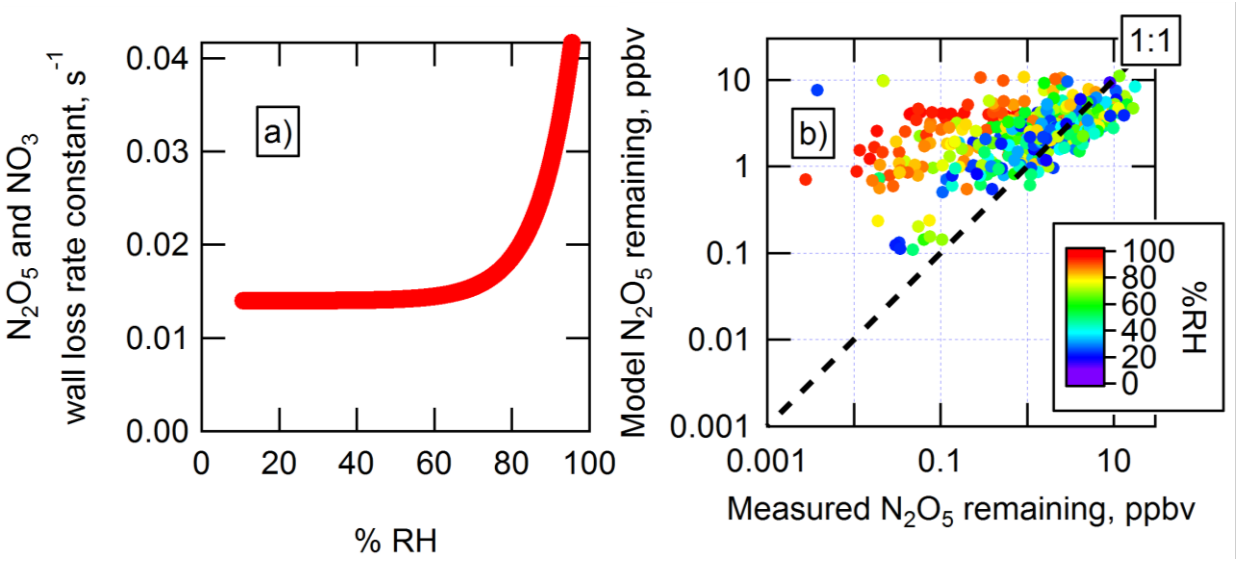

124

125 **Fig. S4.** a) The wall loss rate constant of N_2O_5 and NO_3 vs. %RH, determined empirically in order to
126 achieve agreement between modeled and measured N_2O_5 concentrations (Fig. 2a). b) Modeled vs.
127 measured N_2O_5 remaining (analogous to Fig. 2a), shown if the N_2O_5 and NO_3 wall loss rate was assumed
128 to be a constant 0.014 s^{-1} at all %RH.

129

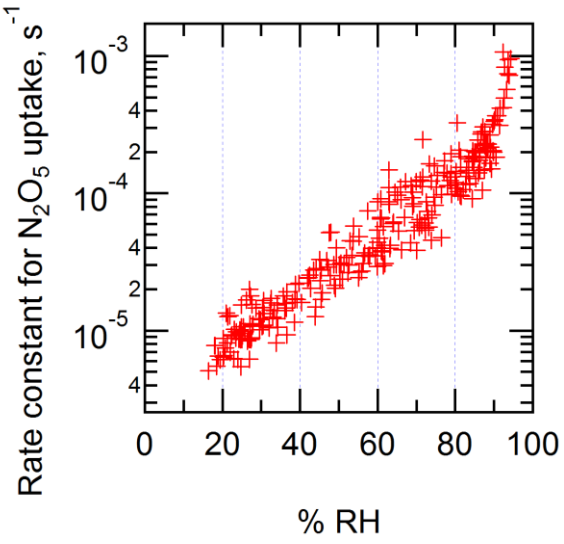

Fig. S5. Calculated rate constant for reactive uptake of N_2O_5 onto particles, as a function of RH. The rate constant was calculated using the same method for condensation of gases onto aerosols described in Palm et al (2016), using the measured ambient aerosol condensational sink and using an organic-mass-fraction-corrected uptake efficiency $\gamma(N_2O_5)$ from Gaston et al. (2014).

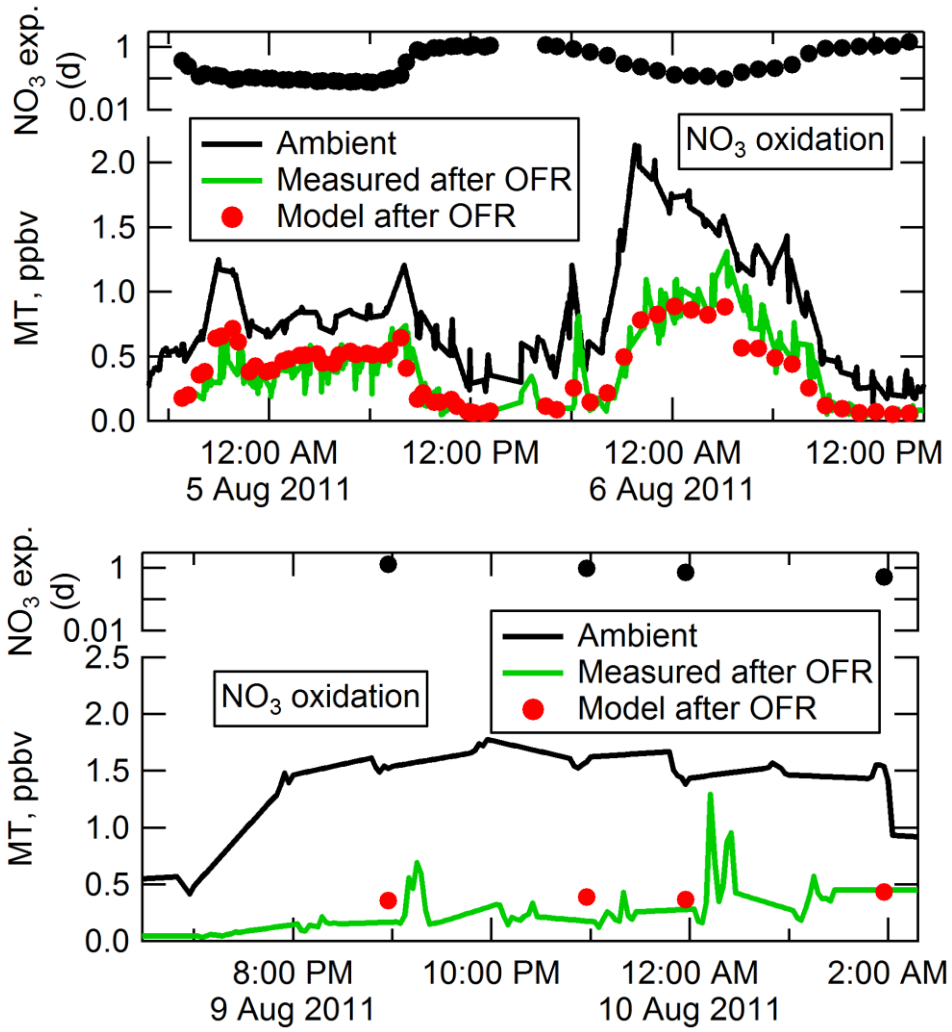

135

136

137 **Fig. S6.** Ambient, measured remaining, and modeled remaining MT from NO_3 oxidation in the OFR on
138 Aug. 4–6 and Aug. 9–10, along with modeled NO_3 exposure (d). For these examples, the amount of
139 injected N_2O_5 was held roughly constant.

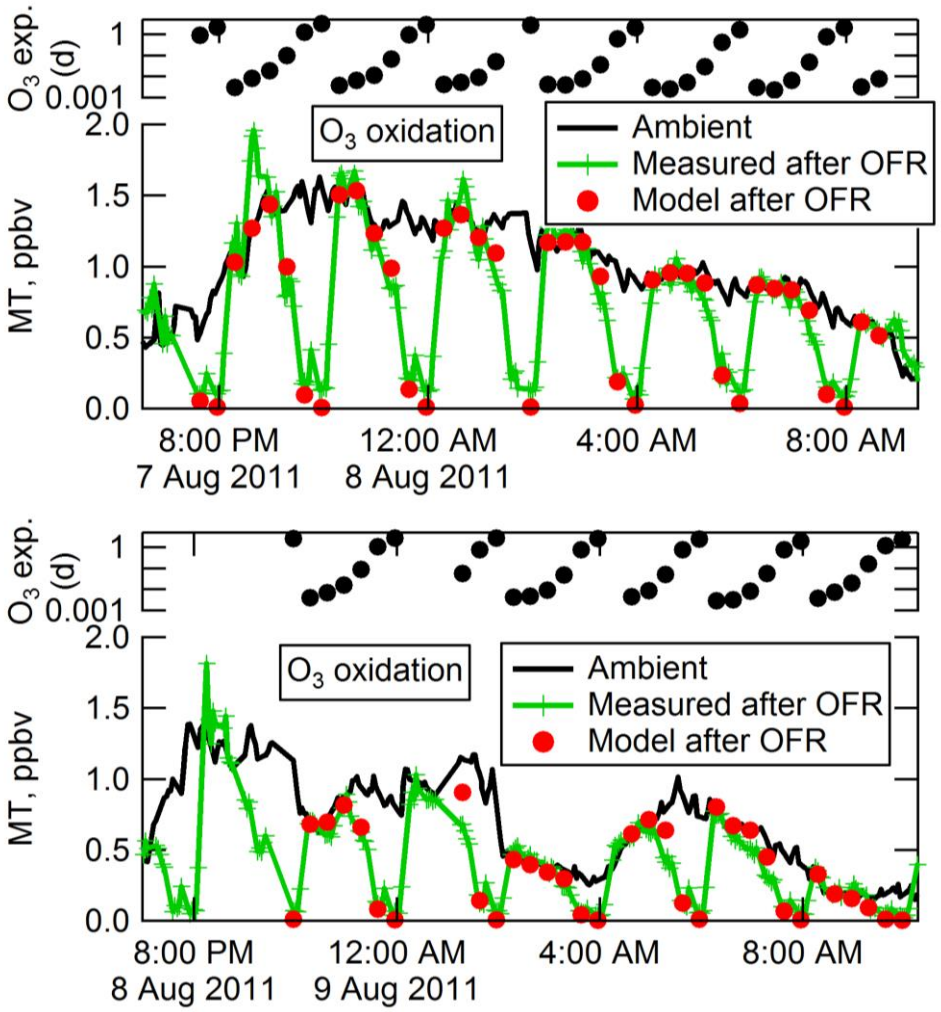

Fig. S7. Ambient, measured remaining, and modeled remaining MT from O_3 oxidation in the OFR on Aug. 7–8 and Aug. 8–9, along with modeled O_3 exposure (d) . The amount of oxidation was cycled from no added oxidant (no MT reacted) to maximum oxidation (most or all MT reacted) in repeated 2–3 h cycles.

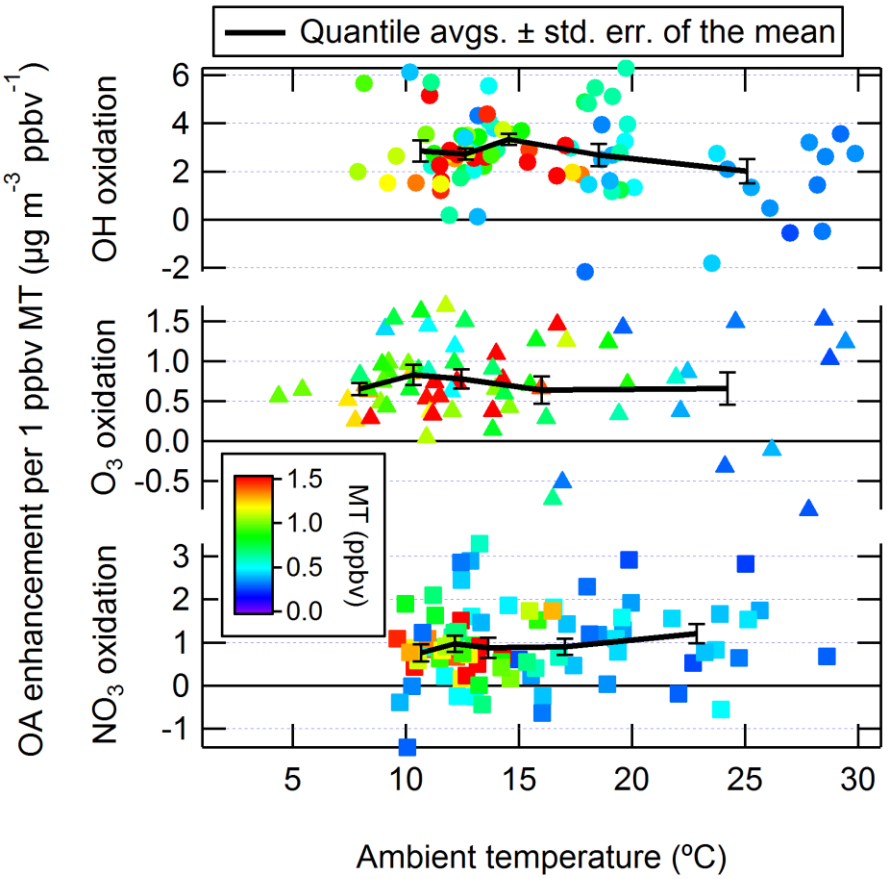

Fig. S8. OA enhancement per ppbv ambient MT for OH, O_3 and NO_3 oxidation in the OFR as a function of ambient temperature. Enhancement is defined as the difference between the concentrations measured after oxidation and in ambient air, where positive enhancements signify formation in the OFR. Data are colored by ambient in-canopy MT concentrations, and include the LVOC fate correction. Quantile averages are shown with error bars corresponding to the standard error of the mean of each quantile.

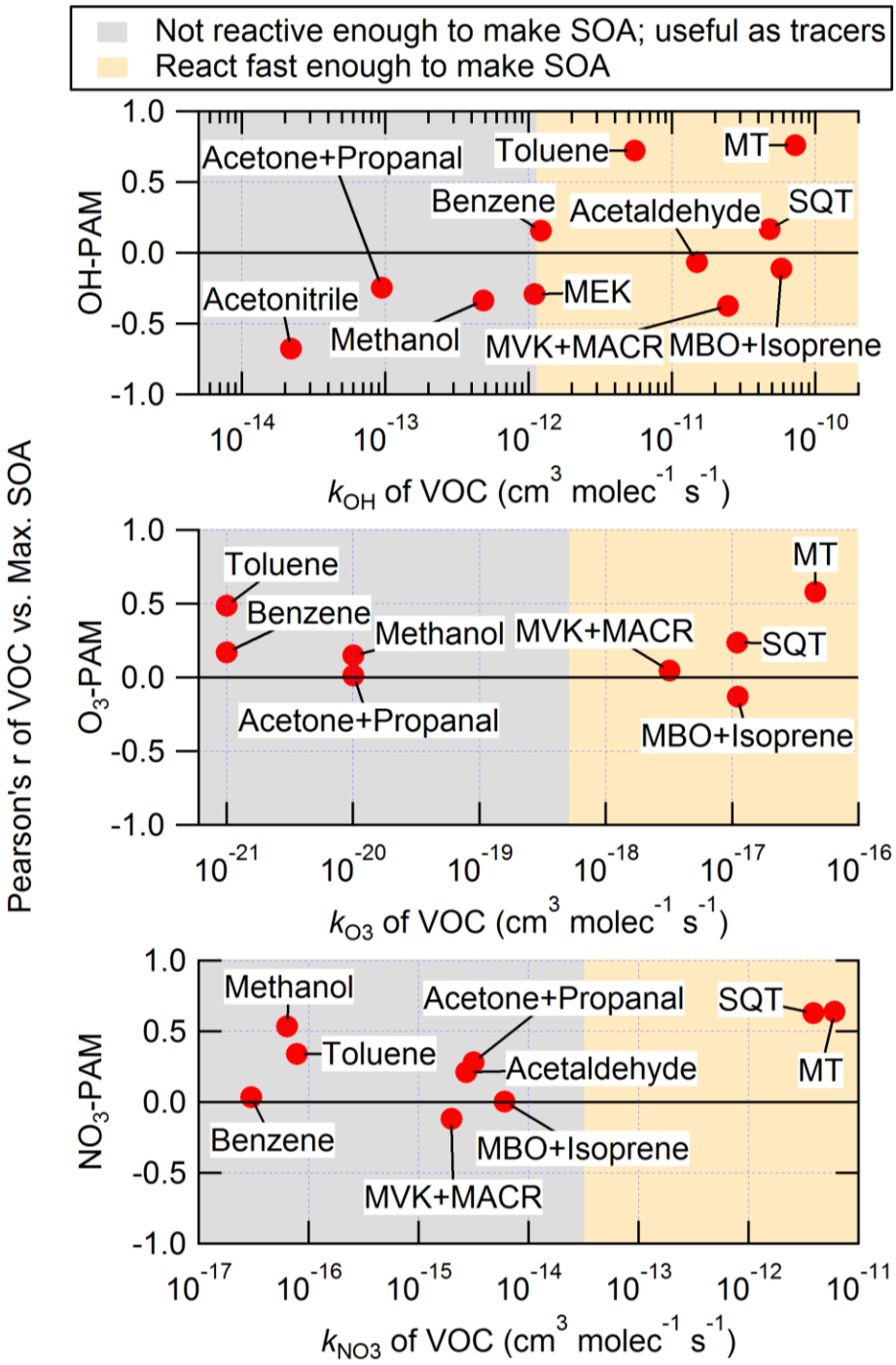

Fig. S9. Pearson's r for the correlation between maximum SOA formation for each oxidant and the available ambient VOC concentrations. Maximum SOA formation is defined as the ranges of 0.4–1.5 eq. d for OH-PAM, 0.7–5 eq. d for O_3-PAM, 0.3–4 eq. d for NO_3-PAM. Reaction rate constants are taken from Atkinson and Arey (2003) and the IUPAC database (Atkinson et al., 2006). The orange colored background denotes rate constants that are fast enough so that ≥20% of the VOC can react to form SOA under the conditions of maximum SOA formation in the OFR for each oxidant. In contrast, the grey background shows rate constants where the molecules do not react in the OFR and cannot contribute to SOA formation, but could be useful as tracers.

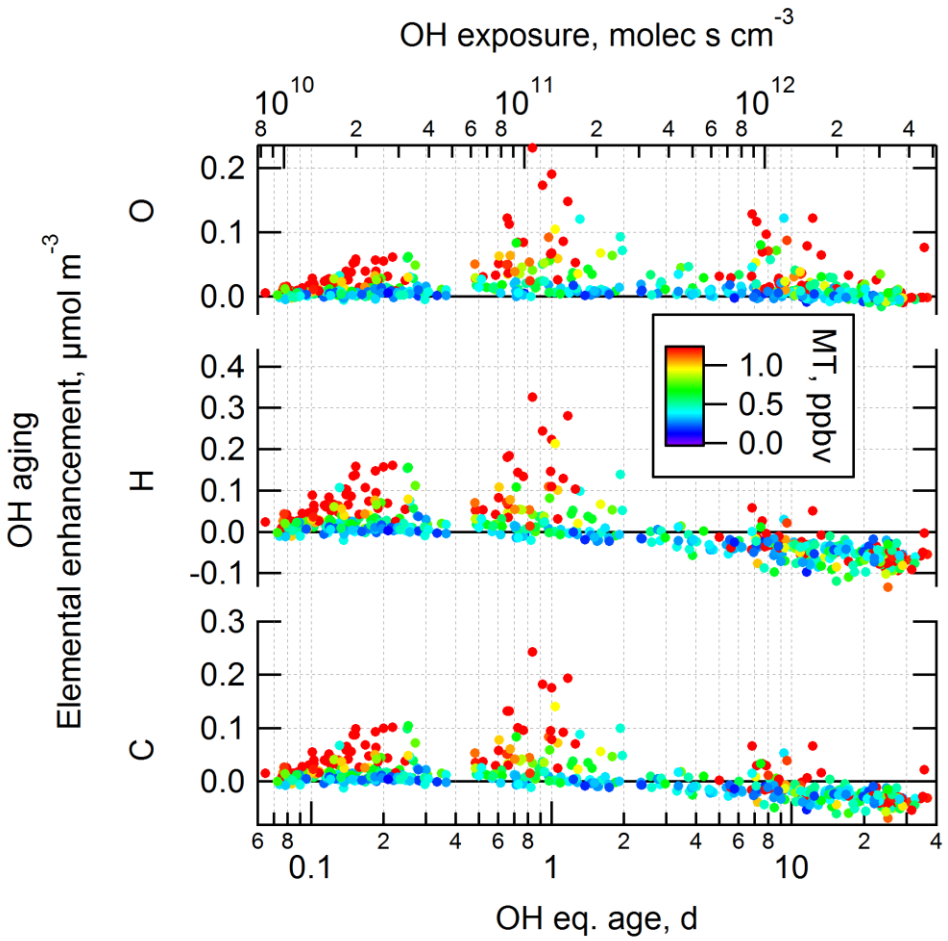

Fig. S10. Elemental C, H, and O enhancements due to OH aging in the OFR, as a function of eq. OH age and exposure. Enhancement is defined as the difference between the concentrations measured after oxidation and in ambient air, where positive enhancements signify formation in the OFR. Data are colored by ambient in-canopy MT concentrations, and do not include the LVOC fate correction.

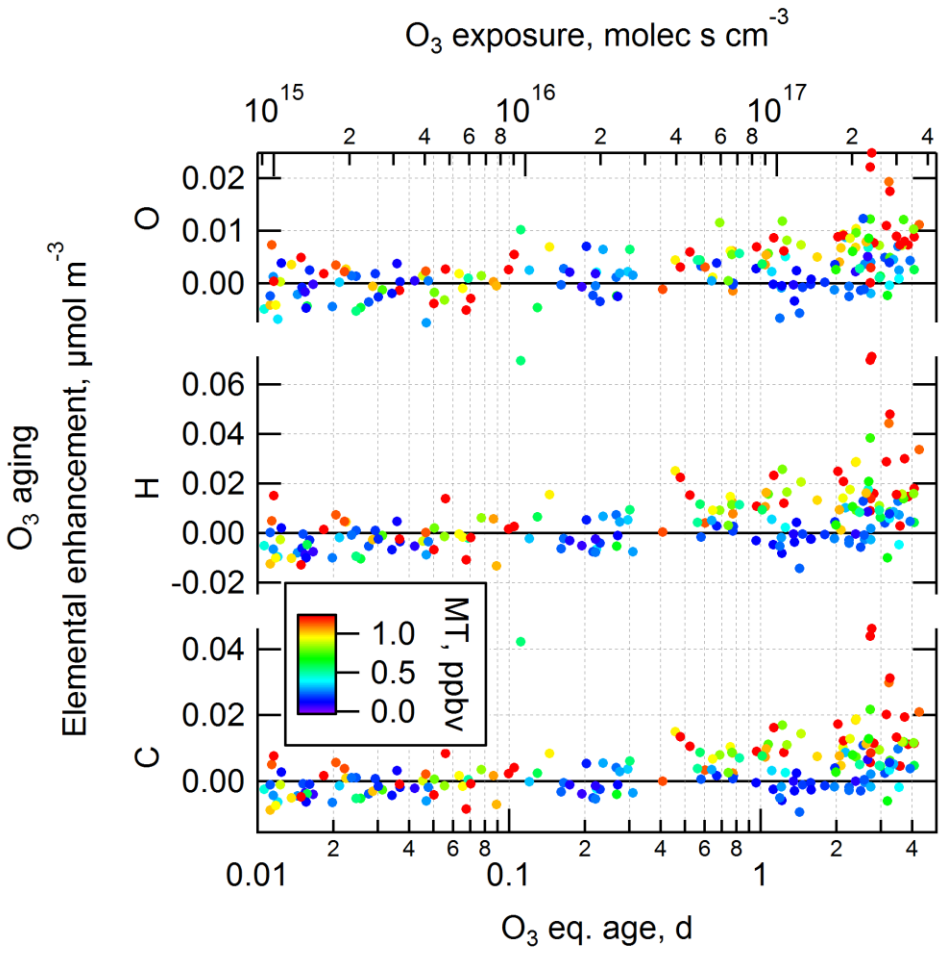

168

169 **Fig. S11.** Elemental C, H, and O enhancements due to O_3 aging in the OFR, as a function of eq. O_3 age and
170 exposure. Enhancement is defined as the difference between the concentrations measured after
171 oxidation and in ambient air, where positive enhancements signify formation in the OFR. Data are
172 colored by ambient in-canopy MT concentrations, and do not include the LVOC fate correction.

173

174

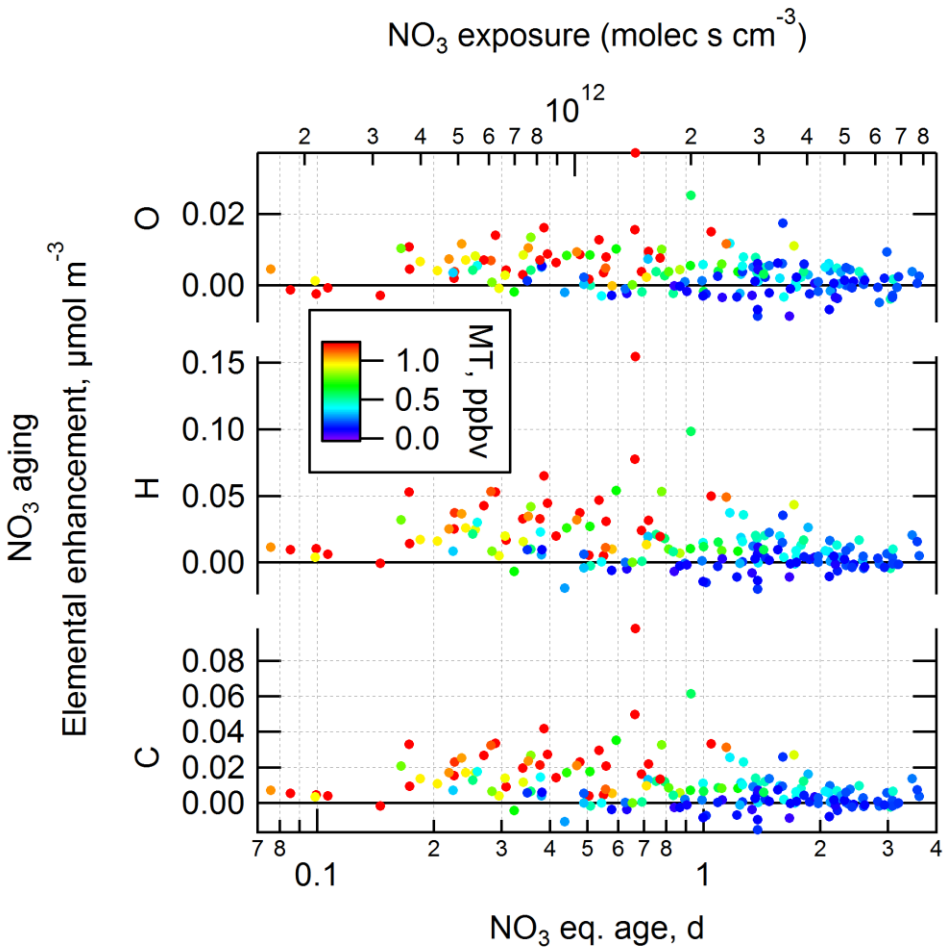

175

176 **Fig. S12.** Elemental C, H, and O enhancements due to NO_3 aging in the OFR, as a function of eq. NO_3 age
177 and exposure. Enhancement is defined as the difference between the concentrations measured after
178 oxidation and in ambient air, where positive enhancements signify formation in the OFR. Data are
179 colored by ambient in-canopy MT concentrations, and do not include the LVOC fate correction.

180

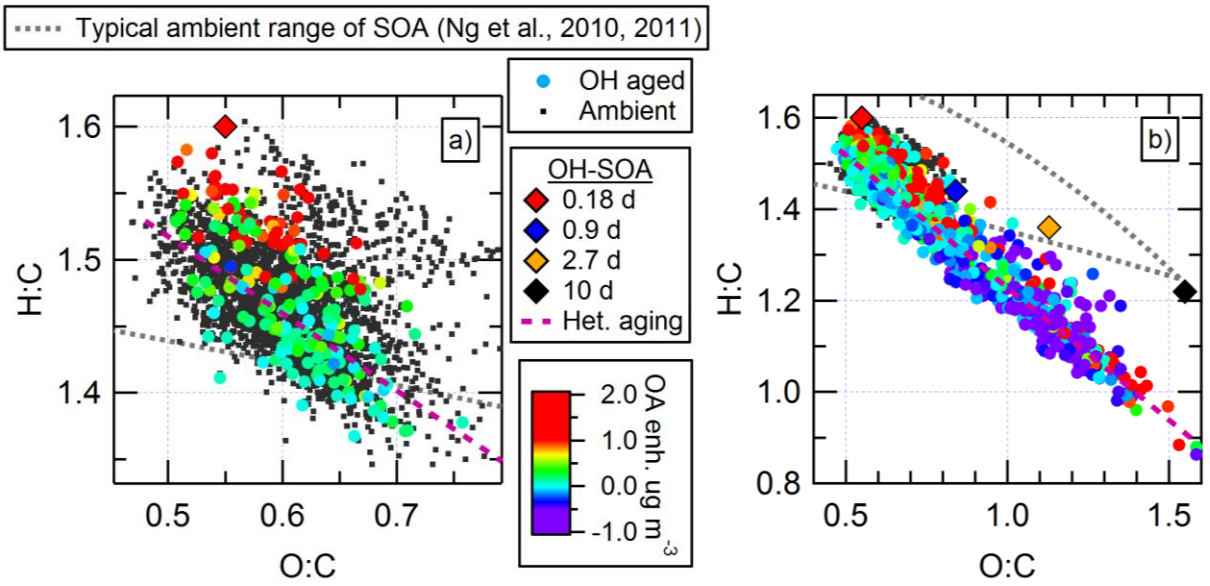

181

182 **Fig. S13.** Van Krevelen diagrams of H:C vs. O:C ratios of OA after OH oxidation of ambient air in an OFR,
183 along with values for ambient OA. OH aged data are colored by the amount of OA enhancement
184 observed after oxidation. The H:C and O:C ratios of the new SOA mass formed in the OFR (i.e., the slopes
185 from Fig. 8) are shown (diamonds; see Fig. 11). For data where no net C addition was observed after OH
186 oxidation, the slope along which heterogeneous OH oxidation transforms the ambient OA is shown
187 (purple dashed line). Panel a) shows only data in the eq. range of 0.1–0.4 (avg.=0.18) d, while panel b)
188 shows all data.

189